Electronic Supporting Information

Charge state-dependent ion condensation near conjugated polymer backbones

Dilara Meli, Quentin Thomas, Nicolas Rolland, Guillaume Freychet, Christina J. Kousseff, Priscila Cavassin, Lucas Q. Flagg, Vincent Lemaur, Abhijith Surendran, Zeinab Hamid, Sophie Griggs, Ruiheng Wu, Rosalba A. Huerta, Isaiah D. Duplessis, Bryan D. Paulsen, Tobin J. Marks, Lincoln J. Lauhon, Iain McCulloch, Lee J. Richter, David Beljonne,* Jonathan Rivnay*

* Correspondence to: jrivnay@northwestern.edu and david.beljonne@umons.ac.be

Contents

Supporting Notes

Section S1 – Organic mixed ionic/electronic conductor (OMIEC) swelling

We expand here the discussion on swelling of OMIECs at different potentials, and on concentration and ion type effects. While the lattice expansion calculated by molecular dynamics (MD) appears to agree remarkably well with experiment when the crystals are doped, it is worth noting that it fails to capture passive (no applied bias) swelling observed almost ubiquitously in glycolated OMIECs. This is likely because it happens on a much longer timescale than what is observable via MD. Consequently, it fails to capture cation mediated doping (expulsion) that is sometimes seen at early charge states in OMIECs. Although in general, cation expulsion is mostly observed in electrolytes with more

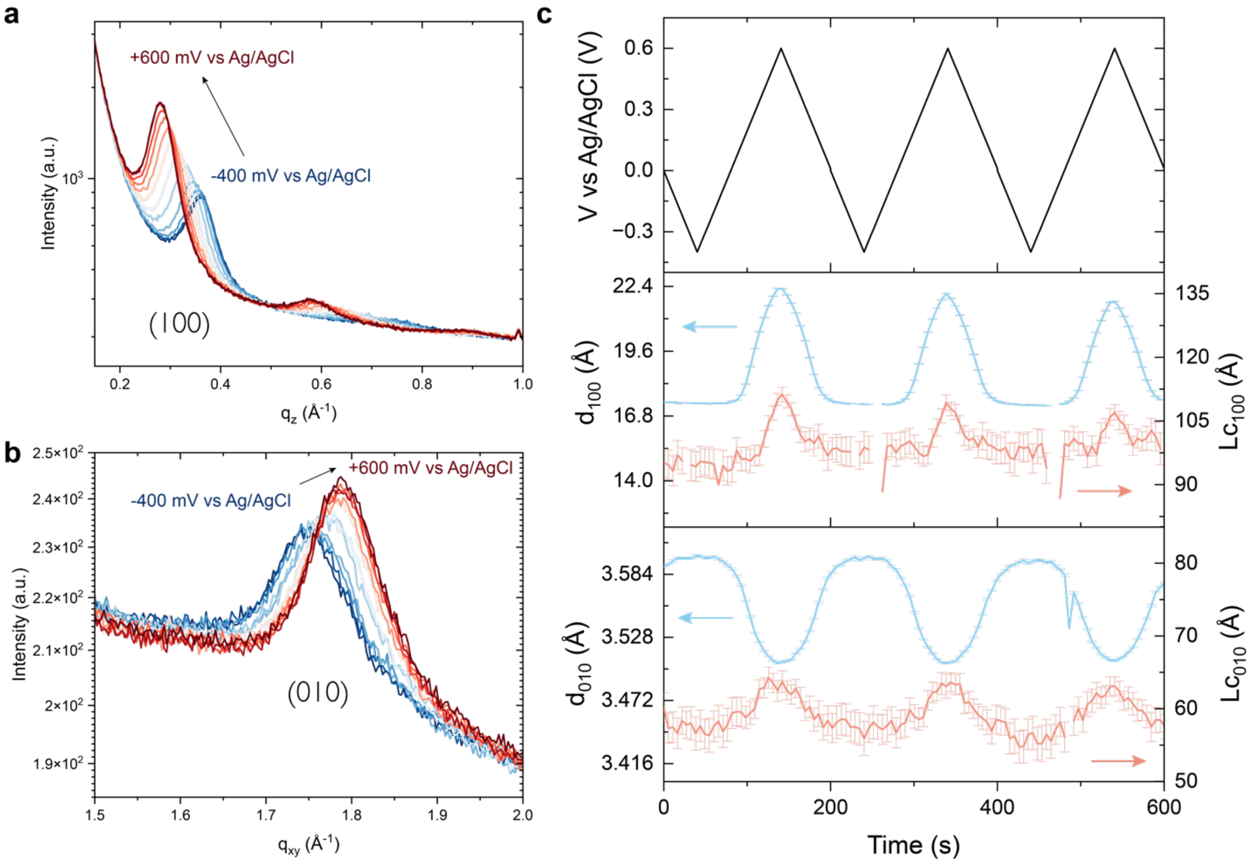

Section S1 Fig. 1. Hard (12.7 keV) operando GIWAXS **a** out-of-plane and **b** in-plane linecuts of first cyclic voltammetry cycle showing lamellar (100) and π-π (010) scattering peaks, respectively. **c** Applied voltage (top) and lamellar peakfits (middle left), lamellar coherence lengths (middle right), π-π peakfits (bottom left) and π-π coherence lengths (bottom right) extracted from linecuts using psudo-Voigt peakfits. pgBTTT was bottom gated in 5 mol L^{-1} NaCl electrolyte. The sweep rate was 0.01 V s^{-1}.

hydrophobic anions (e.g., TFSI$^-$, PF_6^-). We also note here that pgBTTT has been shown to only swell by 16% passively, while other glycolated thiophenes have shown much larger swelling in 0.1 mol L^{-1} NaCl.[1]

The short timescale accessible via MD necessitates high concentration electrolytes (4 mol L^{-1}). As seen in Section S1 Fig. 1, we verified swelling of the crystallite in NaCl at high concentration (5 mol L^{-1}) and observed a similar range of swelling (1.73 to 2.23 nm) as we predicted by MD (1.73 to 2.22 nm) (Tables S1 and S2). However, the majority of aqueous gated OMIECs in literature used 0.1 mol L^{-1} solutions. In addition, $KClO_4$ is not fully soluble in water at 4 mol L^{-1} and even experiments in 4 mol L^{-1} KCl pose a challenge due to the rapid crashing out of salt in ambient conditions. As such, we chose to use 0.1 mol L^{-1} electrolytes for the *operando* GIRXRD experiments. The major differences between experiment and MD are thus larger swelling of experimental crystallites due to increased uptake of water.

Section S2 – Calculating anomalous diffraction intensity

Since pgBTTT crystallites are known to primarily stack in an edge-on orientation (π-stacking in-plane, lamellar stacking out-of-plane), and there is no alignment of crystallites in the substrate plane, we used a cylindrically averaged Debye scattering equation (1) to predict the scattering intensity from the molecular dynamics simulations.[2]

$$I\ (\boldsymbol{Q}) = \sum_{i,\ j=1}^{N} f_i\, f_j^{*} cos\big(Q_z r_{ijz}\big) J_0[r_{ijxy}(Q_x^2 + Q_y^2)^{1/2}] \qquad (1)$$

Where **Q** is the scattering vector, with respective components Q_x, Q_y and Q_z. f_i and f_j are atomic scattering factors for atoms *i* and *j*. r_{ijz} and r_{ijxy} are the axial and radial components of the pair distance array. As the lamellar scattering is in the out-of-plane direction, we take Q_x and Q_y to be 0 and the zeroth order Bessel function becomes 1. Since $cos\ (Q_z\ r_{ijz})$ = $cos\ (Q_z\ r_{jiz})$ we calculate $I\ (Q_z)$= 2 $\Re\big[f_i\ f_j^{*}\ \big] cos\ \big(Q_z\ r_{ijz}\big)$ where r_{ijz} is the pair distance array between all i and j atoms for each atom pair and self (for a total of $\frac{N(N+1)}{2}$ pairings).

For the calculations we remove the electrolyte outside of the lamellae to reduce computational cost. As shown in Section S2 Fig. 1, we first rotate each crystallite about the polymer backbone axis to maximize the non-resonant scattering intensity. Since the MD simulations don't account for substrate effects, polymer rotations during MD trajectories are not physically grounded and as such eliminated during this step to mitigate intensity variations between seeds of the simulation.

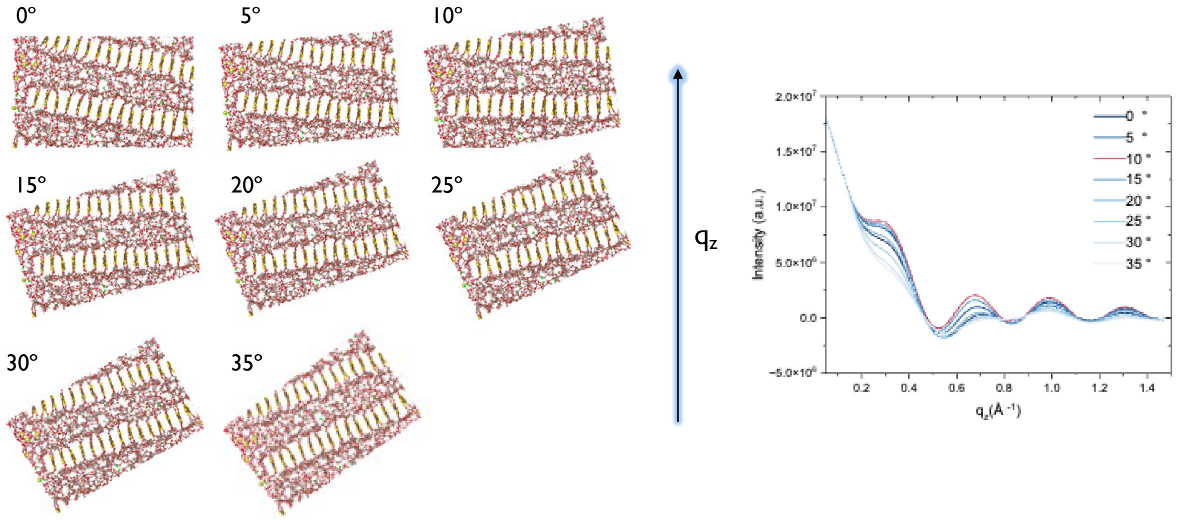

Section S2 Fig 1. Visualization of the non-resonant polymer scattering from MD simulation as a function of rotation about the polymer backbone.

For the resonant calculations, we used the crystallite rotation that maximized non-resonant scattering. The resonant atomic scattering factors were extracted from experiment by flattening the background fluorescence signal (NEXAFS) and normalizing the step edge to 1 using Larch. The normalized signal was then scaled to literature values and interpolated, resulting in *f”*. The interpolated signal was used to generate *f’* using pyElli.

After calculating the resonant scattering as a function of q, we summed the scattering intensity over the q_z range that corresponded to the (100) lamellar scattering. The calculations were averaged over all 25 computational seeds yielding Fig 3c and d.

Section S3 - *Ex situ* humidity experiments

To probe the role of water in facilitating counterion condensation, we studied films doped *ex situ* dry and rehydrated with vapor. The experiments leveraged the same humidity cell used for operando experiments (see Fig. S10) but instead of loading the sample cell that enables liquid electrolyte gating, films were loaded onto a solid metal bar. Prior to loading, the samples were doped in 0.1 mol L^{-1} $KClO_4$. Linecuts of pgBTTT doped at -300 mV vs Ag/AgCl show a slight expansion from q = 0.41 $Å^{-1}$ to 0.34 $Å^{-1}$ (d = 15.5 to 18.3 Å) when the environment is changed to vapor (Section S3 Fig 1a). In contrast, the highly doped film is slightly more expanded in the dry state at q = 0.38 $Å^{-1}$ and expands even further to 0.28 $Å^{-1}$ (d = 16.6 to 22.1 Å) with the addition of vapor.

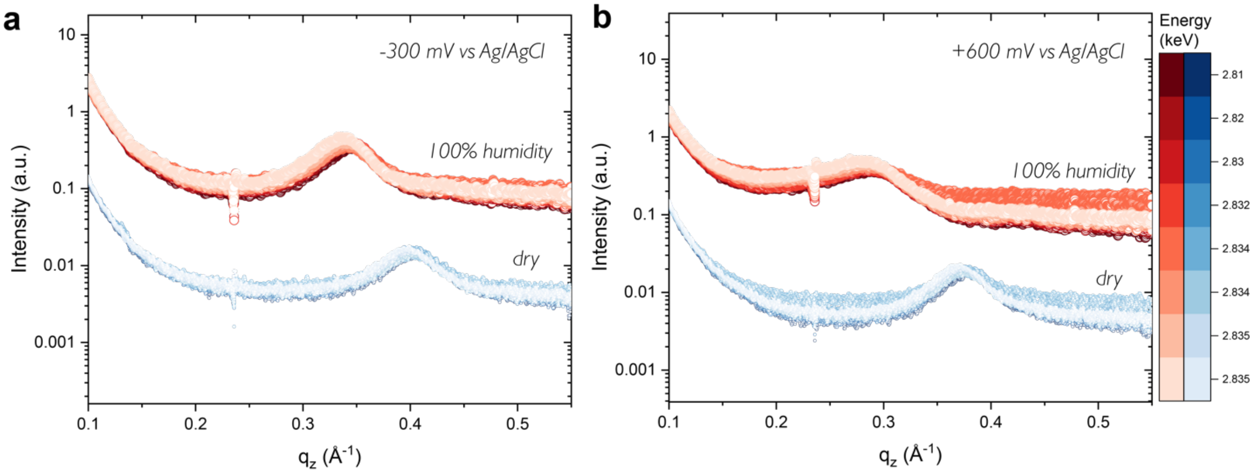

Section S3 Fig. 1 | Linecuts of pgBTTT films *ex situ* doped in 0.1 mol L^{-1} $KClO_4$. Films were doped at **a** -300 mV and **b** +600 mV vs Ag/AgCl. The former represents a lightly doped and the latter a highly doped state (see main text Figure 4 for spectroelectrochemistry data). Both films were first measured under dry N_2 flow at the Cl K-edge. Afterwards, the gas flow was switched to hydrated N_2 and equilibrated for 1 hour and the same films were measured at 100 % humidity. Peaks shown are lamellar (100) diffraction peaks.

Examining the lamellar diffraction intensity across the absorption edge, the signal for the film doped at -300 mV is indicative of counterion ordering near the lamellar mid-plane for both the dry and vapor rehydrated conditions (Supporting Note S3 Fig. 2a). In contrast, while the signal for the highly doped, dry film also indicates ordering near the mid-plane, the signal flips to indicate ordering near the backbone with the change to a vapor environment (Section S3 Fig. 2b).

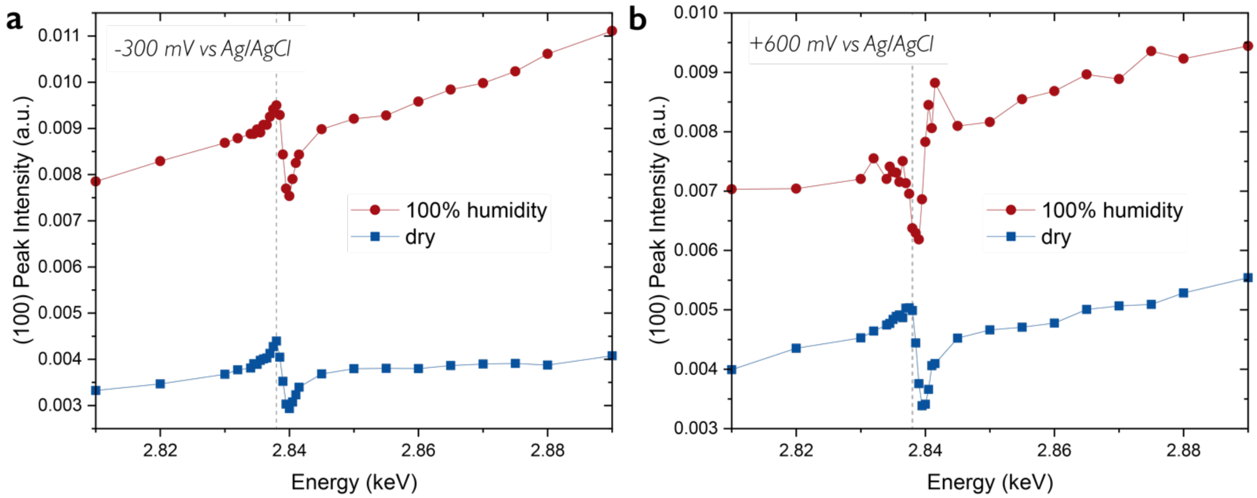

Section S3 Fig. 2 | Lamellar peak intensity across the Cl absorption edge for **a** lightly (-300 mV) and **b** highly (+600 mV vs Ag/AgCl) *ex situ* doped pgBTTT. Both films were first probed under dry N_2 flow before changing to vapor flow. Dotted lines are a guide to the eye.

Section S4 - Extended Methods

Materials synthesis, characterization and sample preparation

Poly(2-(4,4′-bis(2-methoxyethoxy)-5′-methyl-[2,2′-bithiophen]-5-yl)-5-methylthieno[3,2-b]thiophene) (pgBTTT) was synthesized as previously described.[3] The number average molar mass (M_n) was 8.69 kg mol^{-1} and the mass average molar mass (M_w) was 10.84 kg mol^{-1}, resulting in a dispersity of 1.25 as measured by gel permeation chromatography (GPC) using a PLgel 10 μm Mixed-B column on an Agilent Technologies 1260 Infinity system with DMF as the mobile phase at 80 °C. Poly(sodium 4-styrenesulfonate) (NaPSS) (Sigma-Aldrich) was dissolved in DI water at 3 g mL^{-1} before spin-coating onto cleaned glass slides at 524 rad s^{-1} (5000 rpm) to act as a release layer for subsequent float transfer. pgBTTT was dissolved at 5 mg mL^{-} in chloroform and stirred for 10 h at 45 ºC before spin-coating at 26.2 rad s^{-1} (250 rpm) onto NaPSS coated glass slides. 20 μm holes at 120 μm pitch were laser-drilled into 280 μm-thick Si wafers (DSP, University Wafer) to enable electrolyte transport to the polymer films. Chloride experiments used frits with alumina (20 nm) deposited onto undoped Si wafers using ALD to passivate frits, Au working electrodes (90 nm) were deposited using a 10 nm Ti adhesion layer. Perchlorate data used conductive Si frits with two Au working electrodes (50 nm, 5 nm Ti adhesion layer). For operando GIRXRD experiments, polymer films were float-transferred onto porous Si wafers in a room temperature water bath and subsequently annealed at 50 ºC for 20 minutes. For spectroelectrochemistry experiments, films were float transferred onto indium tin oxide (ITO) coated glass slides and similarly annealed at 50 ºC for 20 minutes.

Spectroelectrochemistry

pgBTTT films on ITO coated glass slides were immersed in PMMA cuvette with a 1 cm diameter, 1 mm thick Ag/AgCl pellet (A-M systems). Potential control was carried out with a PalmSens4 potentiostat. Simultaneous absorption spectroscopy was carried out with a halogen white light source (Ocean Optics, DH-2000-BAL) and an optical fiber light path split to separate UV-visible (Ocean Optics, FLAME-S) and near-infrared (Ocean Optics, NQ512) spectrometers. All analysis was carried out using custom Python scripts.

Grazing-incidence resonant X-ray diffraction (GIRXRD)

GIRXRD experiments were conducted at NSLS-II beamline 12-ID (Soft Matter Interfaces). Data were collected on a Pilatus 900 k detector at incidence angles of 0.8 (Cl^-) and 1.6 (ClO_4^-) degrees. *Ex situ* experiments were conducted on samples mounted on a bar with vacuum grease in a vacuum environment. *Ex situ* hydration and *operando* experiments were conducted in a humidity cell that enabled nitrogen flow (dry or wet) while the outside of the cell was kept in vacuum. *Operando* experiments utilized a sample cell that contained a ~3 mL well with an Ag/AgCl R/C electrode. Incident energies were varied to allow for data collection across the Cl^- and ClO_4^- absorption edges; shown RXRD plots of peak intensity versus energy are averages of one up and one down (increasing and decreasing in energy) scan. The energy list for the Cl^- edge was started at 2.803 keV and the ClO_4^- at 2.810 keV to account for a shift in the absorption edge due to the difference in the bonding state of the counterions. Data were analyzed in Python, using smi_analysis and custom code. The sample was shifted by 30 μm between collection points to mitigate beam damage. Out-of-plane line cuts are averages from sector cuts (2-20 degrees) and were fit using a polynomial background and pseudo-Voigt peaks.

Molecular dynamics (MD) simulations

To model ion and water uptake in pgBTTT crystallites by means of classical molecular mechanics (MM) and molecular dynamics (MD) simulations, we employed a well-established workflow to derive an accurate force field for conjugated polymers. This approach has been previously validated for simulating the supramolecular organization of state-of-the-art conjugated polymers such as N2200,[4] IDTBT,[5] pBTTT,[5] DPPDTT.[6] In details, we slightly adapted the Dreiding force field, as implemented in the Materials Studio 2018 package. Namely, the torsion potentials between adjacent polymer subunits, between the conjugated cores and the glycolated chains and along the side chains have been re-parameterised and benchmarked against MP2/cc-pVTZ calculations. The atomic charges of the conjugated cores have been assigned by fitting the electrostatic potential (ESP charges) calculated at the MP2/6-31G** level on an isolated dimer.

For the construction of the central pgBTTT crystallite, a conformational search was first performed to identify its most stable structure using a procedure that has been previously detailed.[4,5] The simulated interlayer distance of the neat crystallite perfectly matches the measured interlayer distance, see Tables S1 and S2, hence validating our forcefield parameterization.

The molecular dynamics simulations[7] of ion and water uptake in pgBTTT crystallites were performed in LAMMPS[8] using the same reparameterized Dreiding force field as in the conformational search. We employed Dreiding functional forms—harmonic bonds and angles, Fourier torsions for backbone and side-chain rotations consistent with our MP2-based reparameterization, and umbrella impropers to enforce out-of-plane planarity. van der Waals interactions were described by a 12–6 Lennard–Jones potential with Lorentz–Berthelot mixing and a 12 Å real-space cutoff, and long-range electrostatics were treated with a particle–mesh Ewald–type solver (target RMS force accuracy 1×10^{-5}). Intramolecular nonbonded interactions followed standard Dreiding conventions (1–2 and 1–3 excluded; 1–4 included without scaling). Water was modeled as SPC/E with shake constraints on the molecular geometry, and the MD time step was 1 fs.

The MD simulations comprised two lamellae, each consisting of 15 polymer chains arranged in a stacked configuration. These lamellae were embedded in an electrolyte solution of either 4 mol L^{-1} NaCl or 4 mol L^{-1} $KClO_4$ in water, enclosed in a periodic simulation box measuring approximately 130 x 40 x 25 $Å^3$. To ensure structural stability, an extensive equilibration process was performed prior to the doping phase. The system was equilibrated at 300 K for 50 ns under NVT conditions using a Nose-Hoover thermostat, followed by 80 ns under NPT conditions at 1 atm and 300K with a Nose-Hoover thermostat and barostat.

During the doping phase, the system was maintained under NPT conditions with the same temperature and pressure. Positive charges were incrementally added to the polymer backbone atoms at intervals of 25 ns. For each doping step, 10 cations (Na^+ or K^+) were removed from the electrolyte, and 10 positive charges were evenly distributed across the sulfur and carbon atoms of the conjugated backbones by fractionally increasing the atomic charge of each atom. A spring constant of 50 kcal mol^{-1} $Å^{-2}$ was applied to constrain the polymer's center of mass, preventing displacement during the doping process. This protocol was repeated across 25 independent simulation seeds for each electrolyte system to ensure statistical significance.

To evaluate the validity of the homogeneous doping assumption, we performed additional simulations employing several heterogeneous doping schemes (**Fig. S20**) using 5 independent simulation seeds per configuration. The insertion behavior of ions and water (**Fig. S21 a & b**), as well as the charge density at which ion condensation occurs, remained unchanged across all cases. The only noticeable difference was a slight decrease in lamellar spacing in the 1–4 and 1–2 configurations (**Fig. S21 c**), relative to the homogeneous case. This variation arises from more localized charge accumulation that induces minor chain misalignment. Overall, these results support the validity of the homogeneous doping assumption used throughout this work.

We compared the energy of a fully separated (“unzipped”) pair of lamellae with that of the two-lamellae stack under identical 4 M KClO4 electrolyte conditions at 0.17 charge per monomer. Using total per-atom potential energies of the polymer backbone, the unzipped state was higher in energy (19.6 kcal mol^{-1} per backbone atom, averaged over 5 independent simulation seeds) than the two-lamellae stack (16.5 kcal mol^{-1} per backbone atom, averaged over 25 simulation seeds). Accordingly, unzipping is not energetically favored under our conditions, consistent with the absence of spontaneous separation over the simulated timescales.

Post-simulation data analysis was conducted in Python, with MDAnalysis[9,10] being one of the main tools used. OVITO[11] and VIAMD[12] were extensively used as visual tools to qualitatively validate the structural trends observed in the Python analysis. Radial distribution functions were calculated using the tool directly implemented in MDAnalysis.

For density maps, the analysis pipeline processed trajectories to extract ion positions, compute radial distributions, align structures to reference configurations, and track structural changes and ion localization within cylindrical regions. Atom counts were performed by generating 3D convex surfaces around the crystallites using an alpha shape algorithm to track the number of ions and water molecules entering the lamellae. These species were then further classified based on their spatial proximity to the polymer backbone (condensated, midchain, or outside), and their coordination environments were quantified by computing the number of nearby atoms within defined inner (4 Å) and outer (6 Å) coordination spheres. The energetic landscapes were derived by computing the potential of mean force as a function of the minimum distance between chloride ions and the polymer backbone. For each time step of the molecular dynamics simulations, the closest distances between each anion and all backbone atoms were calculated. These normalized distance distributions were then converted into free energy profiles using Boltzmann inversion, according to $PMF(r) = -k_B T \ln P(r)$, where $P(r)$ is the probability density of observing an ion at distance r. Because Boltzmann inversion relies on a well-sampled distribution of configurations, the use of 25 independent simulation seeds was essential to ensure sufficient statistical coverage. This procedure yields a one-dimensional projection of the effective interaction landscape between ions and the polymer. To isolate electrostatic contributions, each 25-ns doping stage was reprocessed with LAMMPS in rerun mode using the original coordinates and charges. Van der Waals interactions were set to zero, and per-atom potential energies were computed from pair and long-range electrostatics only. Analysis was focused on the center of the lamellae to minimize edge effects and better represent bulk-like behavior. For each 1-ns window within a doping stage, the per-site electrostatic energy was first time-averaged over different realizations and both lamellae, for each backbone atom of the three central chains, and the spatial variance across backbone sites was then computed. We considered the 15 equilibrated windows of every stage (windows 11–25 within each 25-ns block). For each window index and stage we aggregated across seeds to obtain the mean and standard error of the mean. Displacement of chains in the π-stack from planarity in the lamellar direction was assessed by computing the center-of-mass positions of the conjugated backbones in the (x, y) plane, where x corresponds to the π–π stacking direction and y to the 100 lamellar axis. For each half-lamella, a linear regression was performed along the π–π axis, and orthogonal deviations from the fitted line were calculated along the 100 direction for each chain. The probability distributions of these displacements were then compiled separately for each doping level.

GIRXRD calculations

GIRXRD calculations were executed using custom Python code. Atom positions were read in from .cif files resultant from MD simulations, and coordinate frames were rotated between 0º and 35º in 5º increments around the polymer backbone to mitigate effects due to tilting of the backbone during the evolution of the MD trajectory. Pair-wise distance arrays were calculated using MD Analysis.[9,10] Atomic scattering factors for non-resonant atoms were taken from literature.[13] For Cl^- and ClO_4^- f'' was generated using experimental data from the background region of the 2D detector to obtain μ (E) using the Larch XAS GUI,[14] and then scaled to literature values in the pre- and post-edge regions. f' was calculated from f'' using pyElli and similarly scaled to literature values.

Supporting Figures

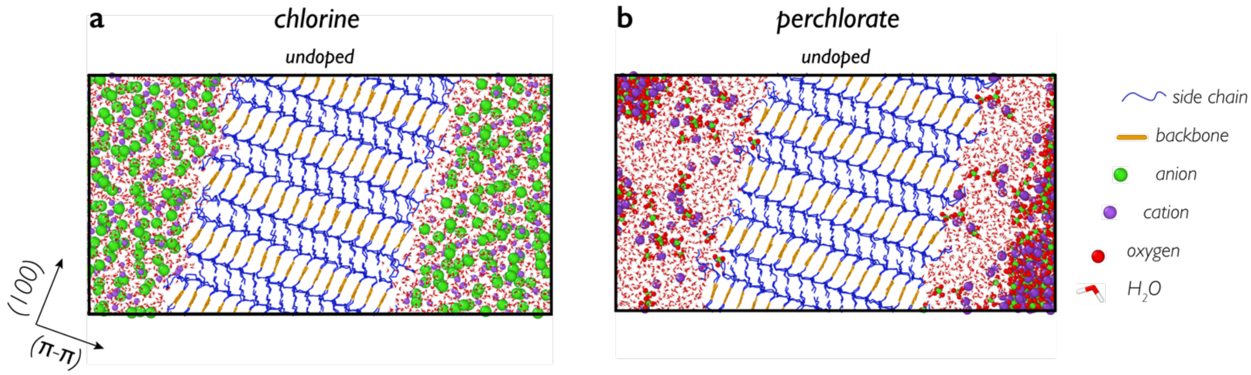

Figure S1. Equilibrated starting configuration of MD simulations prior to doping in 4 mol L^{-1} **a** NaCl and **b** $KClO_4$ electrolytes. Glycolated side chains are shown in blue, polymer backbones in orange, anions (Cl^-, ClO_4^-) in green, cations (Na^+, K^+) in purple, oxygen in red and water as red and white elbow shapes. The snapshots replicate one repeat of the simulation box in the (100) direction for clarity and were rendered using Ovito.[11]

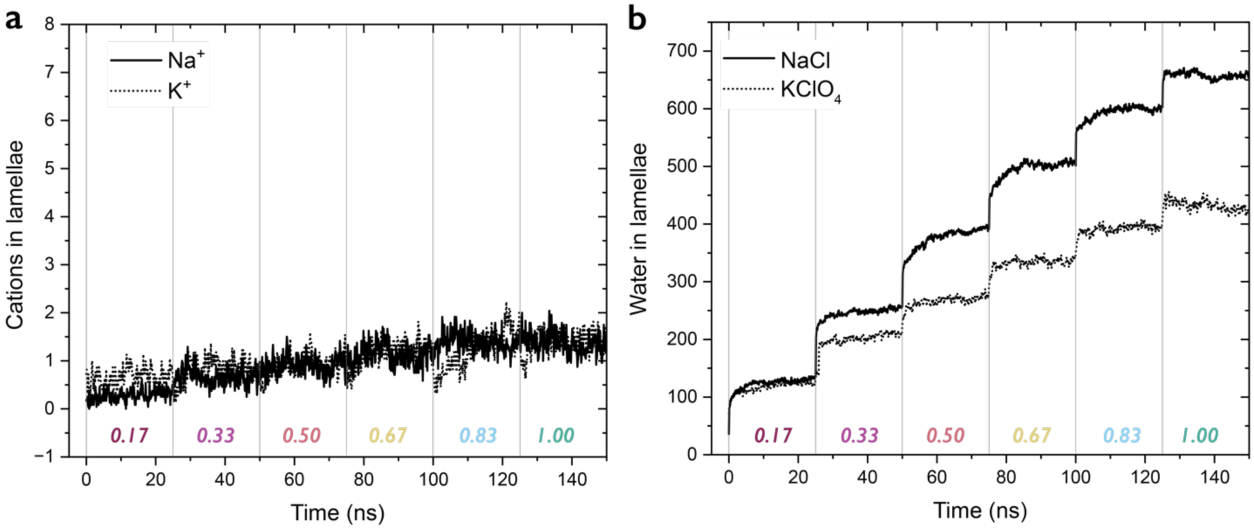

Figure S2. Cation insertion into lamellae during MD charging. Na^+ are from NaCl simulations and K^+ from $KClO_4$ simulations, both at 4 mol L^{-1}. **b** Total water insertion into lamellae during MD charging. Decimal fractions reflect charge per monomer (or per 4 thiophenes).

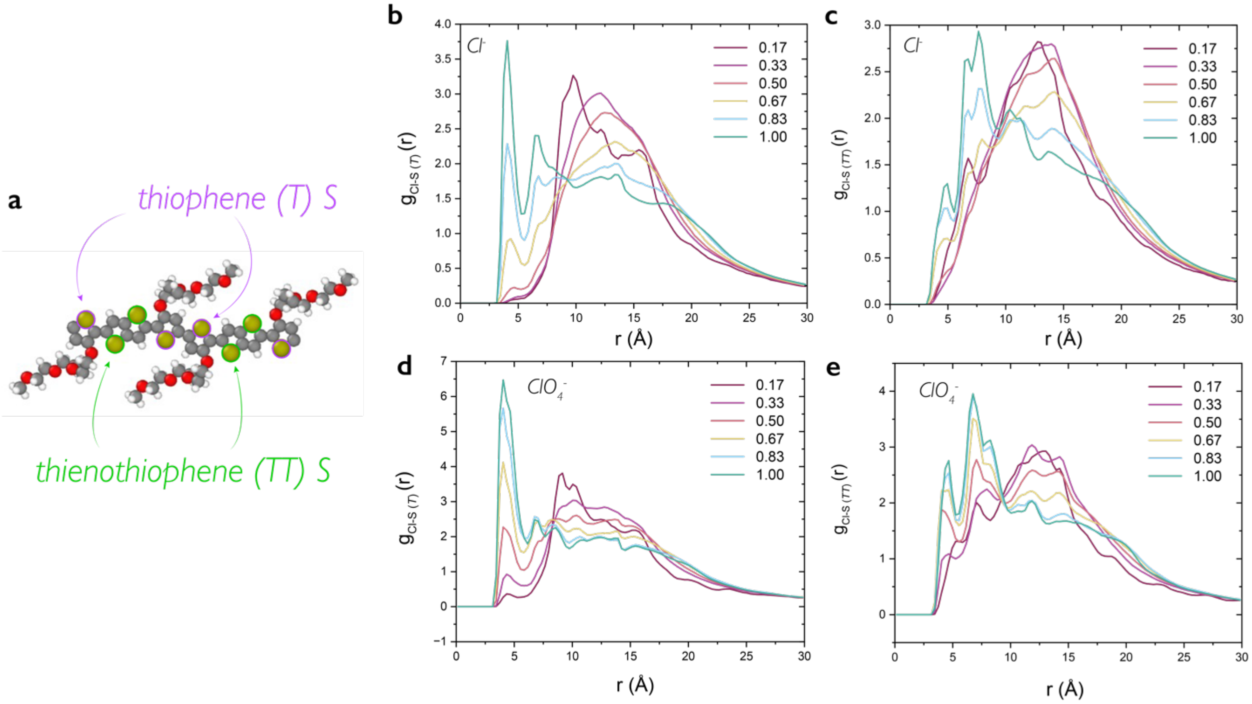

Figure S3. a schematic of a pgBTTT dimer highlighting thiophene (T) and thienothiophene (TT) sulfur atoms. **b** Radial distribution functions, *g (r)*, of chlorine and thiophene (T) sulfur atoms and **c** *g (r)* of chlorine and thienothiophene (TT) sulfur atoms. **d** Radial distribution functions, *g (r)*, of perchlorate Cl and thiophene (T) sulfur atoms and **e** *g (r)* of perchlorate Cl and thienothiophene (TT) sulfur atoms. Decimal fractions reflect charge per monomer (or per 4 thiophenes).

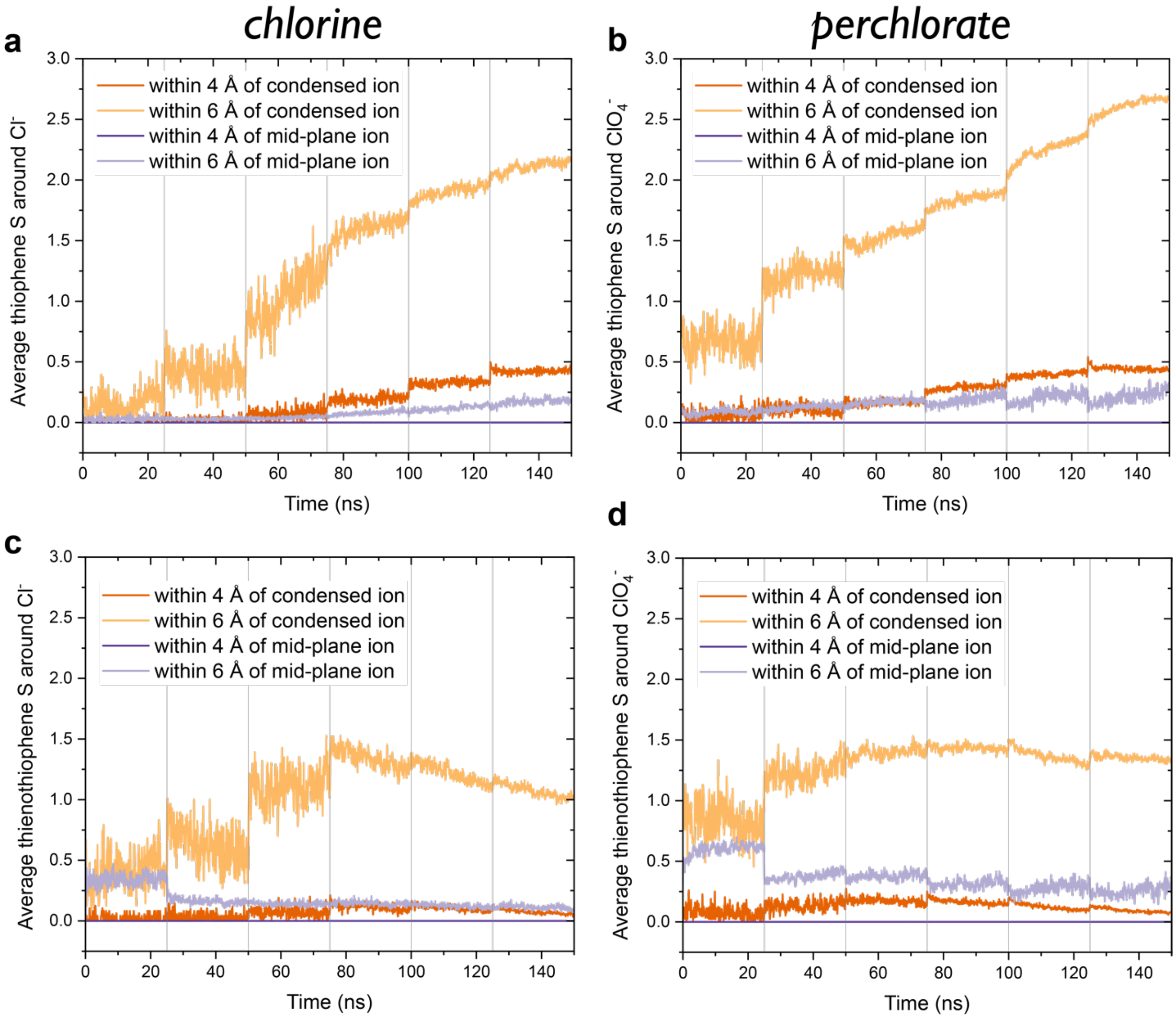

Figure S4. Coordination environments of condensed and mid-plane ions during charging. Number of thiophene S atoms within 4 Å and 6 Å around **a** Cl$^-$ and **b** ClO$_4^-$ ions and number of thienothiophene S atoms within 4 Å and 6 Å around **c** Cl$^-$ and **d** ClO$_4^-$ ions. The 4 Å shell includes atoms (0 to 4) Å away from the ions and the 6 Å shell includes atoms (0 to 6) Å around the ions. All curves are averaged across 25 independent simulation seeds. Ions are considered “condensed” if Cl$^-$ are within 4.8 Å and if ClO$_4^-$ within 4.5 Å of the polymer backbone.

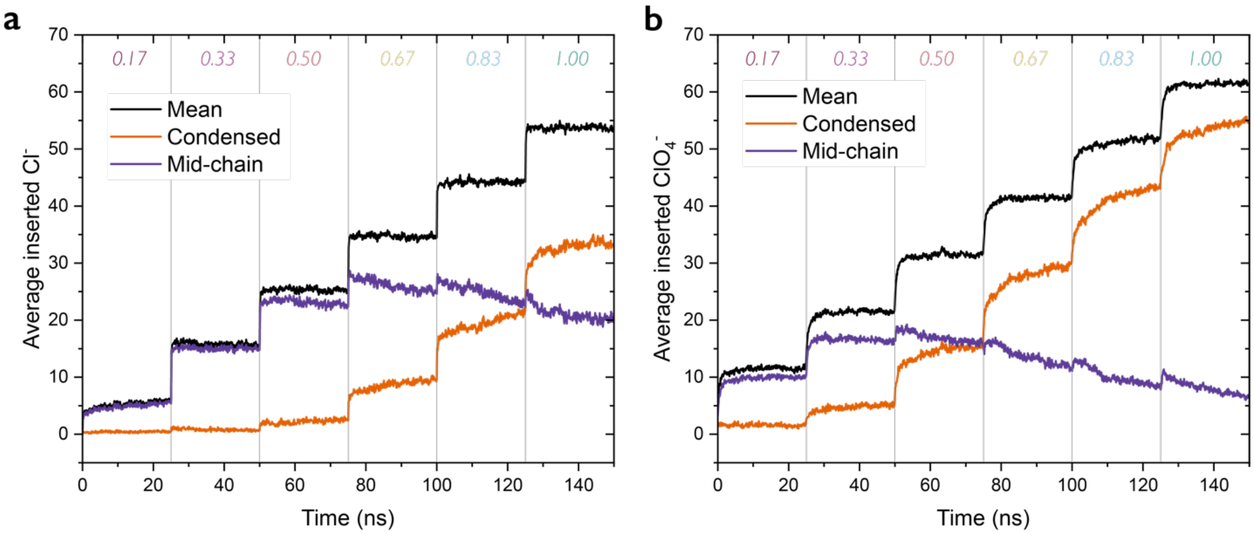

Figure S5. Counterion uptake between lamellae as a function of charge separated by location where the ions localize for **a** Cl^- and **b** ClO_4^-. All curves are averaged across 25 independent simulation seeds. Ions are considered "condensed" if Cl^- are within 4.8 Å and if ClO_4^- within 4.5 Å of the polymer backbone. Cutoff criteria were determined using main text Fig. 5a and Fig. S18. Decimal fractions reflect charge per monomer (or per 4 thiophenes).

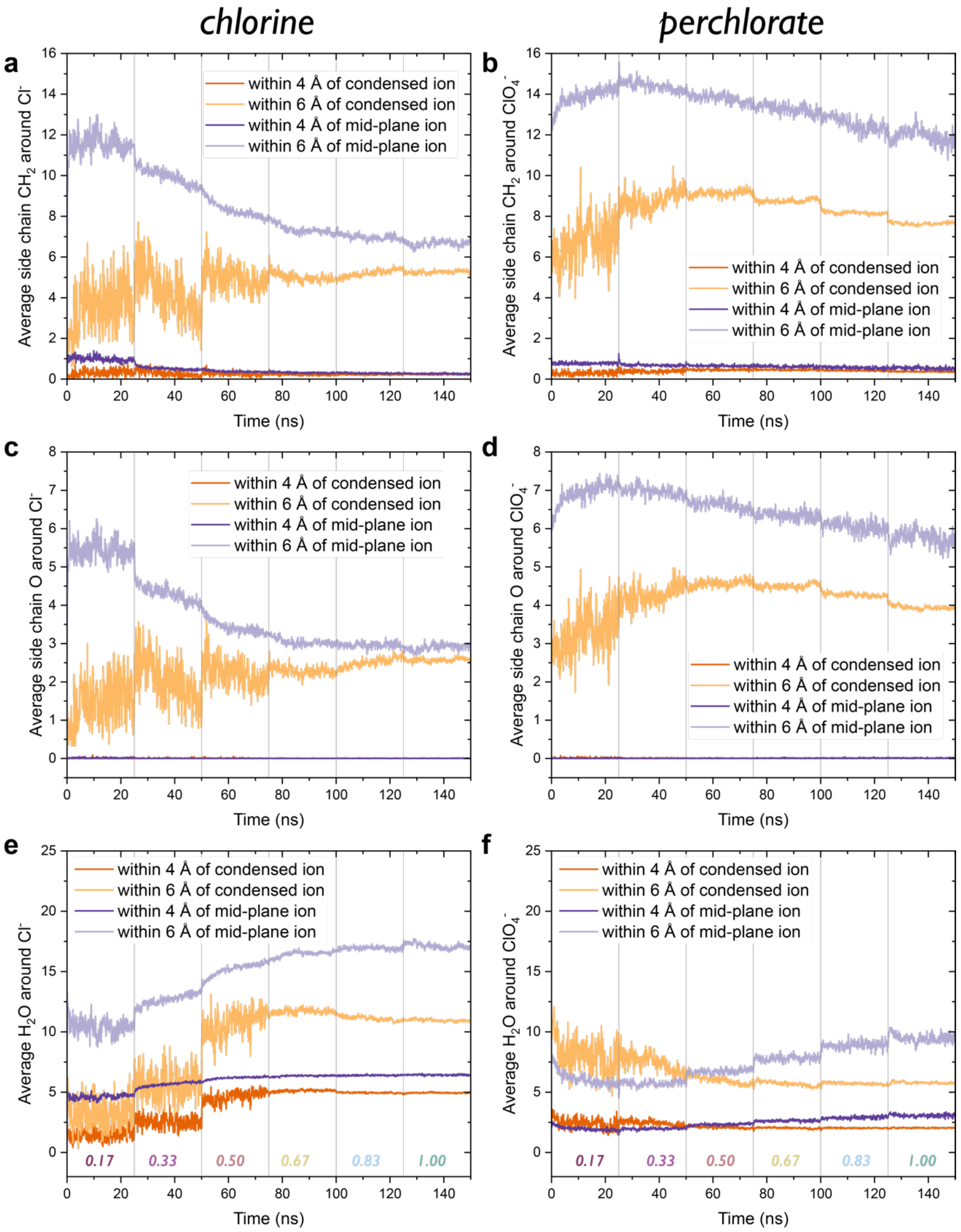

Figure S6. Coordination environments of condensed and mid-plane ions during charging. Number of side chain CH_2 groups within 4 Å and 6 Å around **a** Cl^- and **b** ClO_4^- ions, number of ether O atoms within 4 Å and 6 Å around **c** Cl^- and **d** ClO_4^- ions, and number of water molecules within 4 Å and 6 Å around **e** Cl^- and **f** ClO_4^- ions. The 4 Å shell includes atoms (0 to 4) Å away from the ions and the 6 Å shell includes atoms (0 to 6) Å around the ions. All curves are averaged across 25 independent simulation seeds. Ions are considered "condensed" if Cl^- are within 4.8 Å and if ClO_4^- within 4.5 Å of the polymer backbone. Decimal fractions reflect charge per monomer (or per 4 thiophenes).

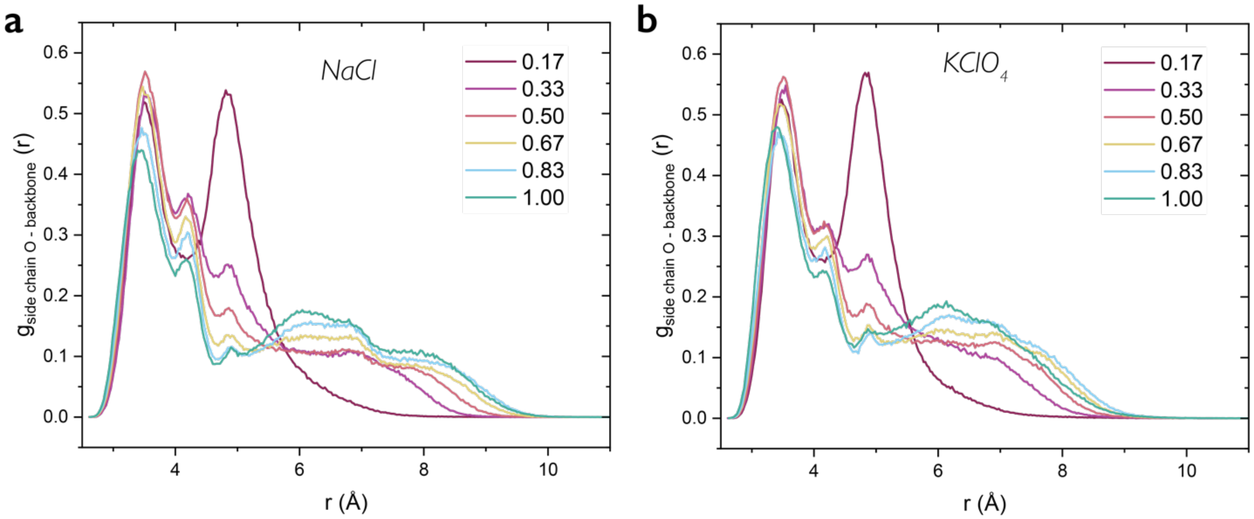

Figure S7. Radial distribution function, *g (r)*, of side chain oxygen atoms with the polymer backbone for **a** NaCl and **b** $KClO_4$ simulations. All curves are averaged across 25 independent simulation seeds. Decimal fractions reflect charge per monomer (or per 4 thiophenes).

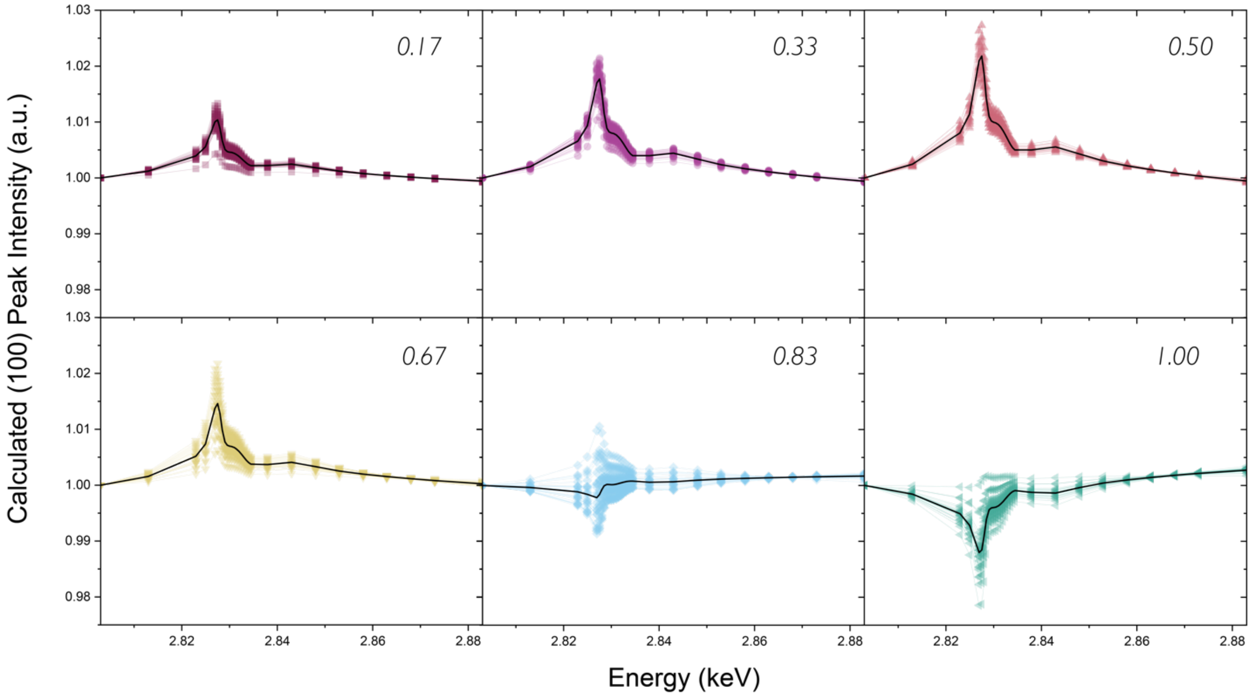

Figure S8. Calculated (100) peak intensity from molecular dynamics simulations for Cl^- anions for all simulation seeds. Overlaid black curves are averages as shown in main text Fig. 3c. Decimal fractions reflect charge per monomer (or per 4 thiophenes).

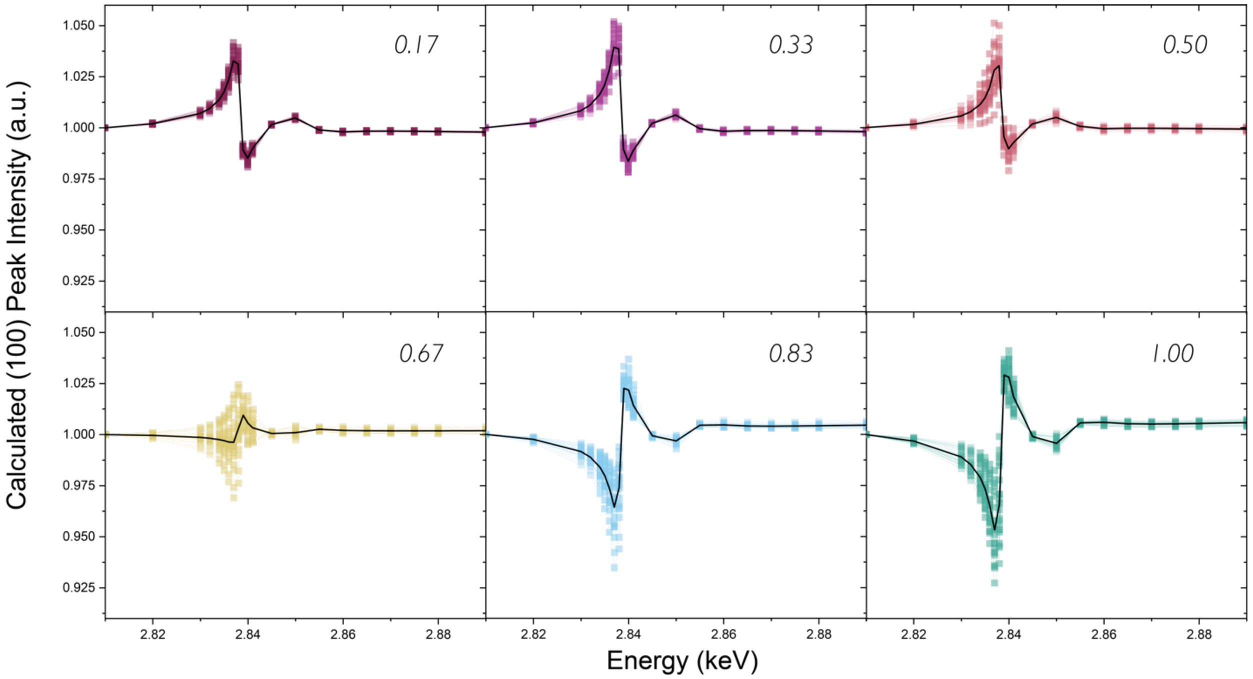

Figure S9. Calculated (100) peak intensity from molecular dynamics simulations for ClO_4^- anions for all simulation seeds. Overlaid black curves are averages as shown in main text Fig. 3d. Decimal fractions reflect charge per monomer (or per 4 thiophenes).

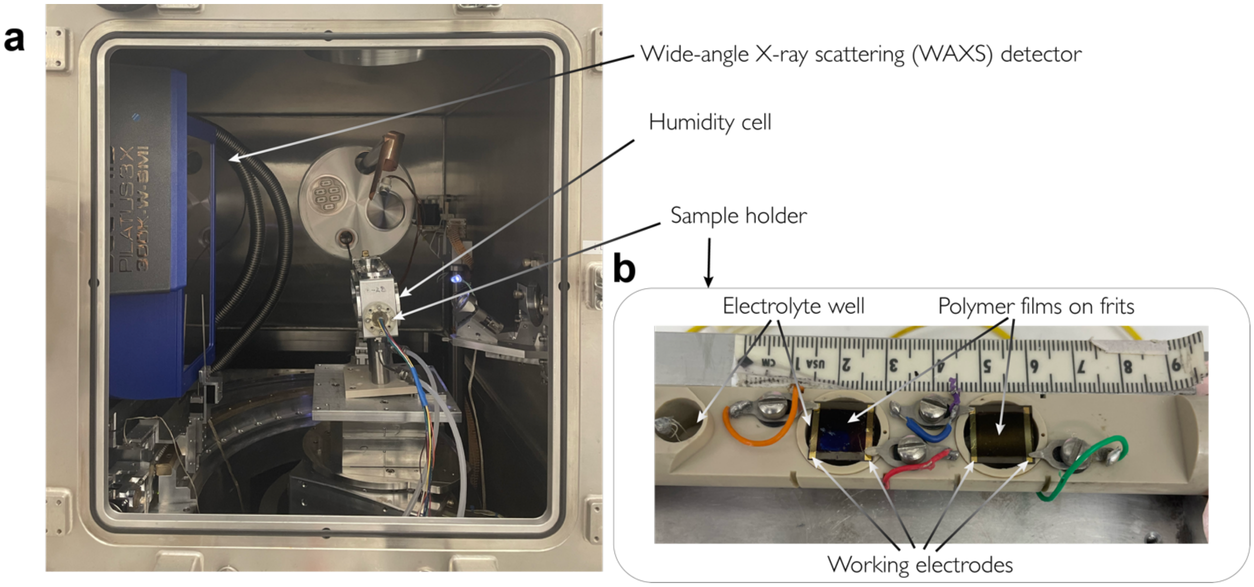

Figure S10. GIRXRD experimental setup. **a** Photo of open vacuum chamber at NSLSII beamline 12-ID (SMI). Highlighted are the wide-angle X-ray scattering (WAXS) detector on which the data is collected, the humidity cell that enables (hydrated) gas flow while the chamber is purged as well as the sample holder that inserts into the humidity cell. **b** Top down view of the sample holder with labeled electrolyte well that contains Ag/AgCl R/C electrodes, labeled working electrodes and polymer films on porous Si first.

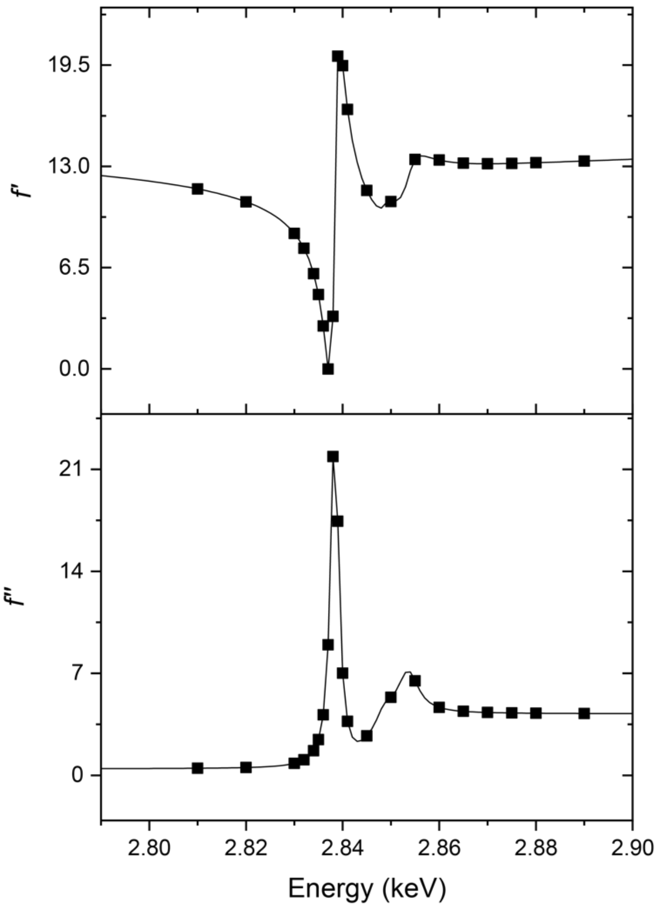

Figure S11. Real (top) and imaginary (bottom) parts of the ClO_4^- atomic scattering factor extracted from experiment. Overlaid scatter plot shows sampling across the absorption edge.

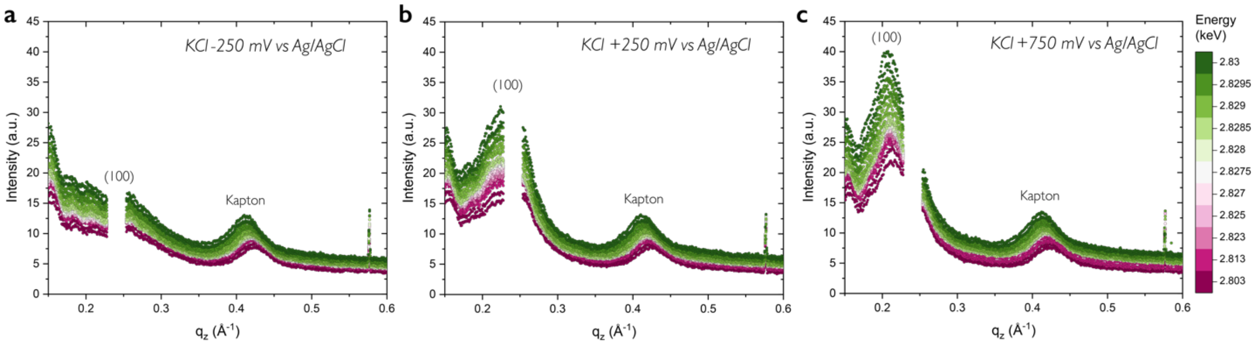

Figure S12. Out-of-plane linecuts of pgBTTT as a function of incident energy in 0.1 mol L^{-1} KCl electrolyte at **a** de-doped (-250 mV), **b** mid-doped (+250 mV), and **c** highly doped (+750 mV vs Ag/AgCl) charge states with labeled lamellar (100) diffraction peaks and Kapton peaks from the humidity cell windows. Gaps in data at ~0.23 $Å^{-1}$ are due to the dead space of the detector. Zingers at ~0.575 $Å^{-1}$ are artifacts.

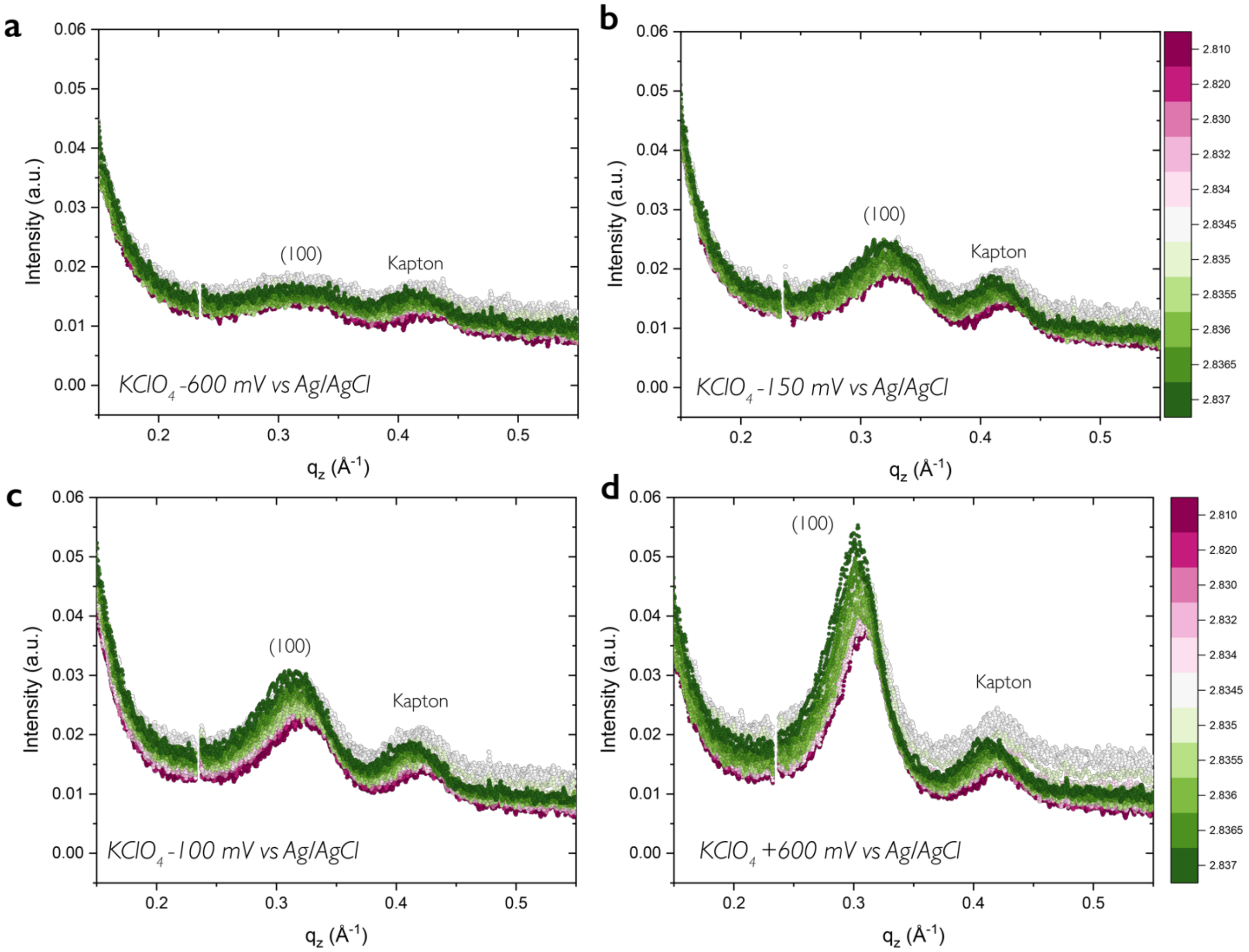

Figure S13. Out-of-plane linecuts of pgBTTT as a function of incident energy in 0.1 mol L^{-1} $KClO_4^-$ electrolyte at **a** de-doped (-600 mV), **b & c** mid-doped (-150 and -100 mV, respectively) and at **d** highly doped (+600 mV vs Ag/AgCl) potentials. Lamellar (100) and Kapton peaks form the windows of the humidity cell are labeled.

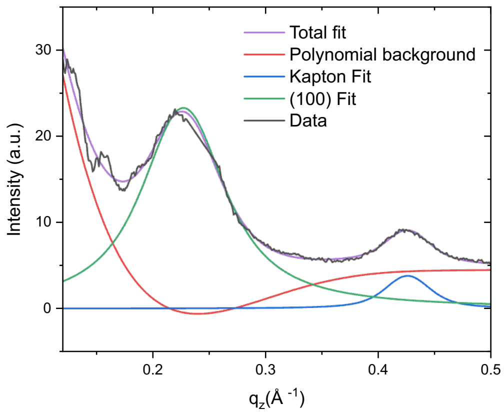

Figure S14. Sample fit to out-of-plane linecuts.

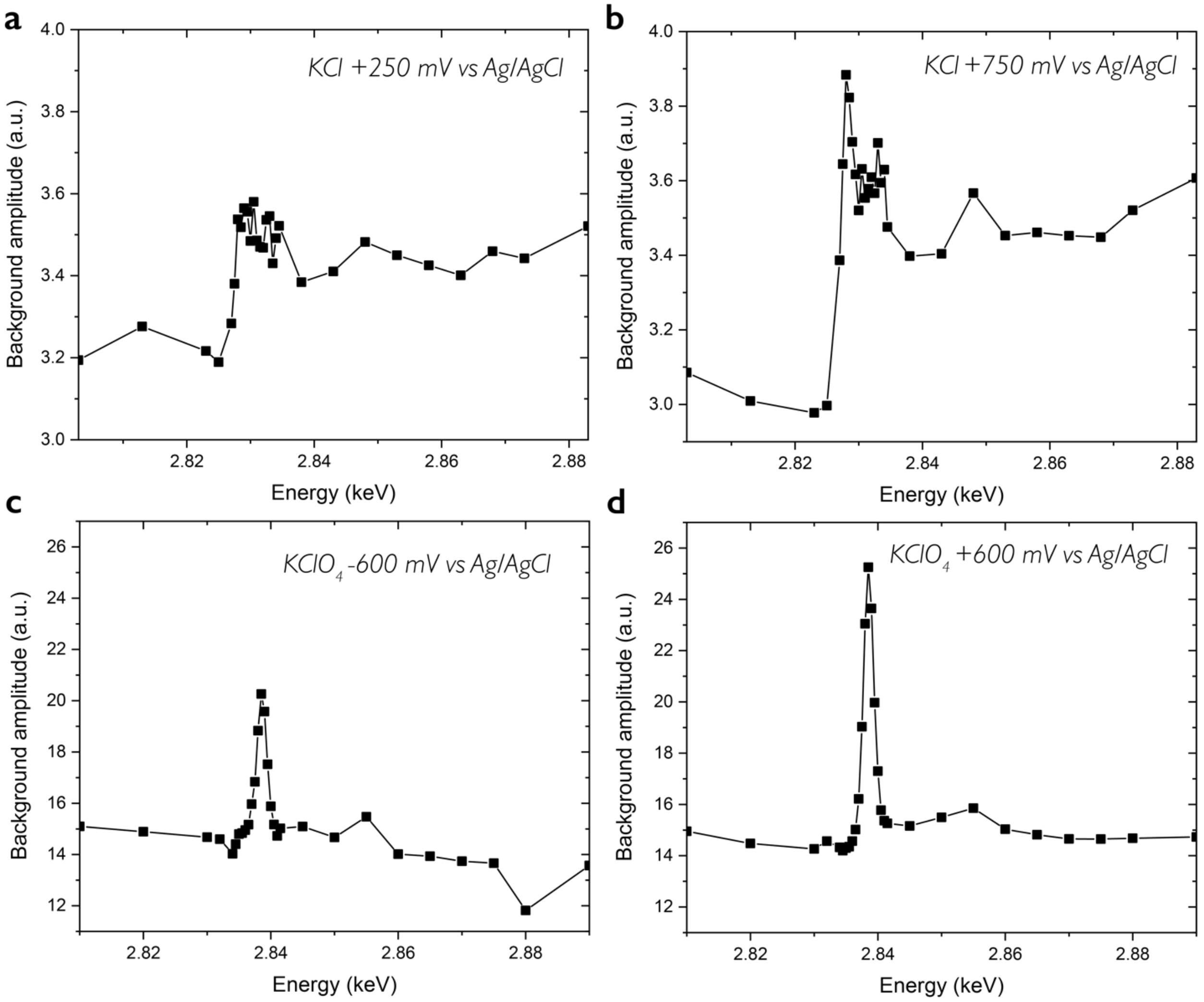

Figure S15. Background amplitude extracted from linecuts for **a** mid-doped and **b** highly doped pgBTTT in KCl and for **c** de-doped and **d** highly doped pgBTTT in $KClO_4$.

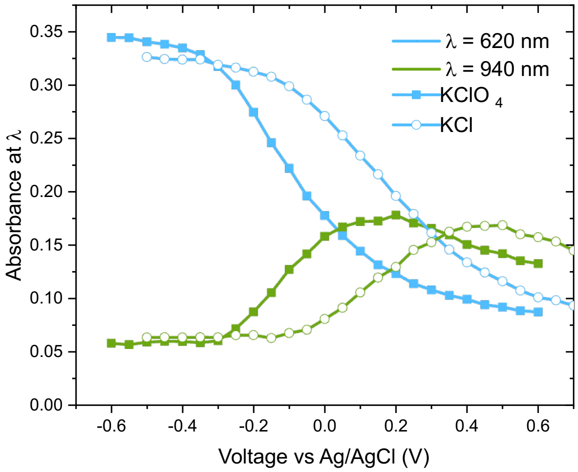

Figure S16. Absorbance of neutral (λ = 620 nm) and polaronic (λ = 940 nm) peaks as a function of applied voltage showing shifted onset of doping in $KClO_4$ electrolyte compared with KCl.

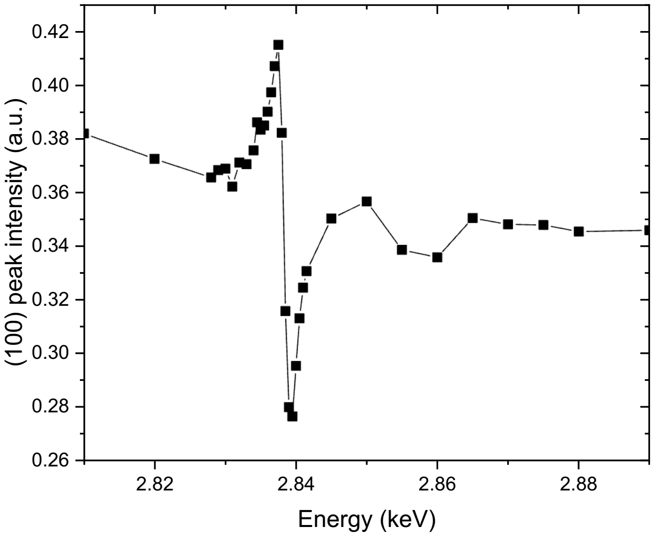

Figure S17. (100) peak intensity from *ex situ* GIRXRD experiments of pgBTTT doped in 0.1 mol L^{-1} in $KClO_4$ electrolyte to +600 mV vs Ag/AgCl.

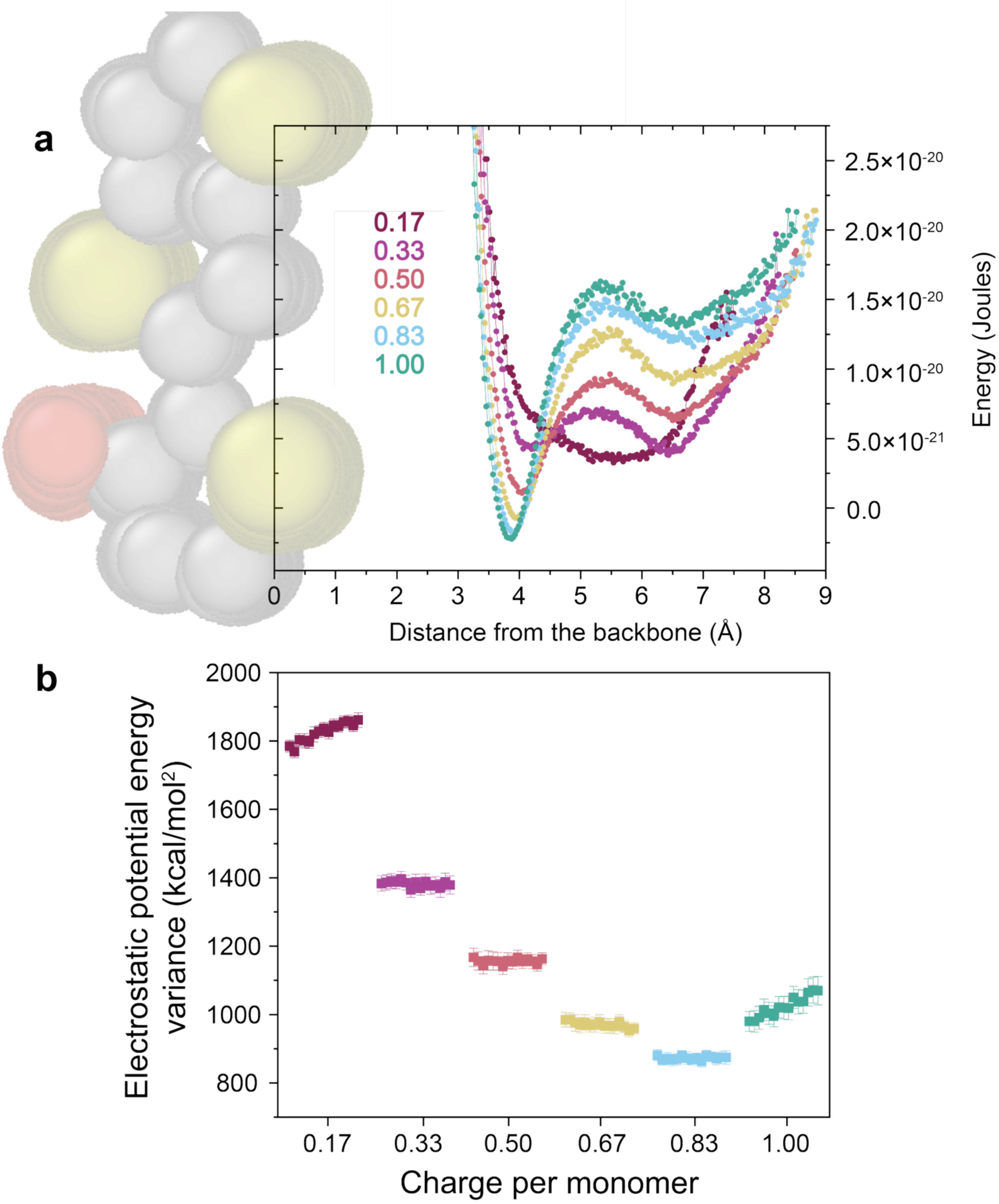

Figure S18. Energetic landscape felt by ClO_4^- ions in the lamellae. Data is cropped at the mid-plane for clarity, snippet of backbone shown for scale. **b** Electrostatic disorder in the central chains of the ClO_4^- doped lamellae, quantified by spatial variance as a function of doping step. For each 1-ns window, the per-site electrostatic energy was time-averaged and its variance across backbone sites was computed for the three central chains within the lamellae. The 15 equilibrated windows (within each 25-ns stage) are plotted consecutively.

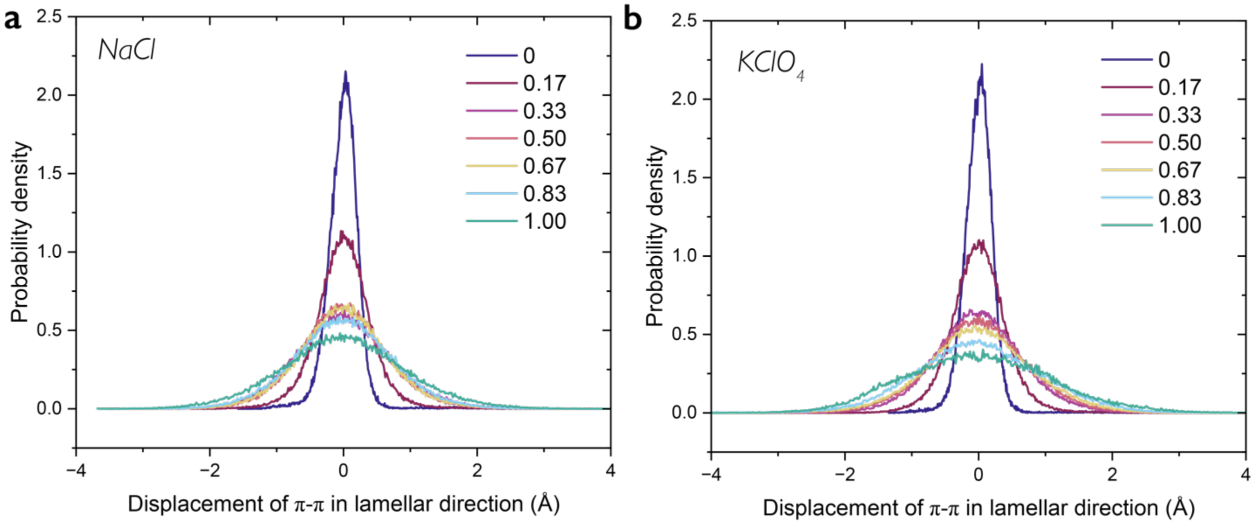

Figure S19. Displacement of chains in the π-stack from planarity in the lamellar direction as a function of charge state for **a** NaCl and **b** $KClO_4$ simulations.

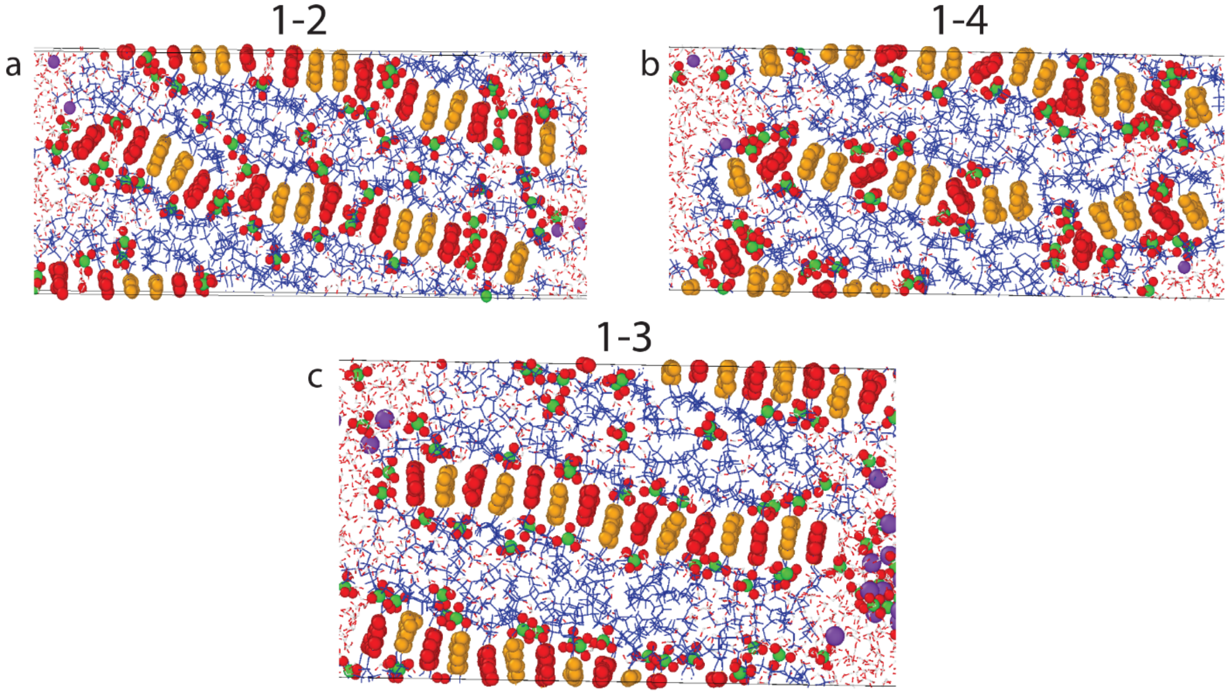

Figure S20. Snapshots from MD simulations of polymer crystallites at 1.0 charge/monomer in $KClO_4$ electrolytes, illustrating three different modes of heterogeneous lamellar doping labelled “1-2”, “1-4” and “1-3” (**a–c**). Red chains represent doped polymers, while orange chains correspond to undoped ones.

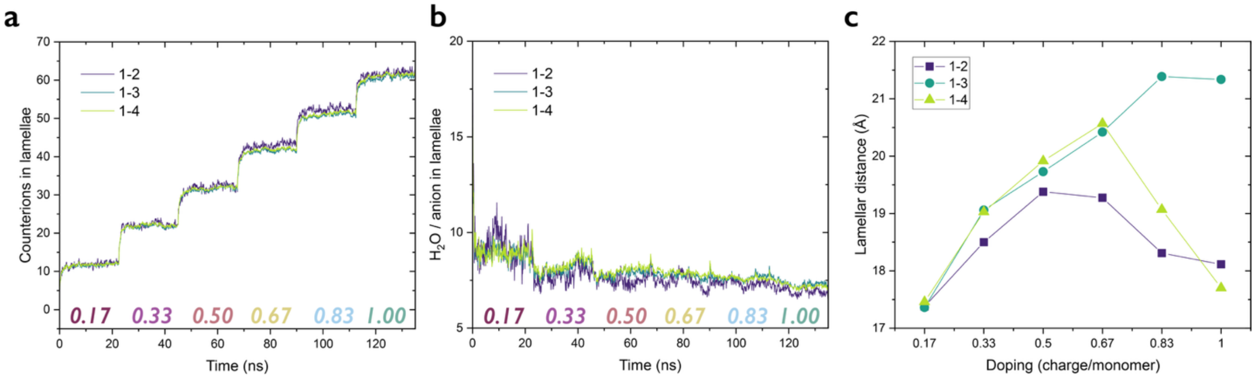

Figure S21. Counterions inserted between heterogeneously doped lamellae (**a**), water to anion ratio (**b**) and lamellar expansion in Angstrom (**c**) during sequential charging steps averaged across 5 simulation seeds for the three different modes of heterogeneous lamellar doping for perchlorate electrolytes. Decimal fraction indicates relative charge per monomer.

Supporting Tables

Table S1. Lamellar expansion extracted from molecular dynamics simulations.

Doping state (%)	**d_{100} (nm) in 4 mol L^{-1} NaCl**	**d_{100} (nm) in 4 mol L^{-1} $KClO_4$**
0	1.73	1.73
17	1.79	1.76
33	1.97	1.91
50	2.06	1.97
67	2.16	2.03
83	2.22	2.03
100	2.21	1.97

Table S2. Lamellar expansion extracted from operando GIWAXS experiments.

V_g vs Ag/AgCl (mV)	**d_{100} (nm) in 5 mol L^{-1} NaCl**	**V_g vs Ag/AgCl (mV)**	**d_{100} (nm) in 0.1 mol L^{-1} KCl**	**V_g vs Ag/AgCl (mV)**	**d_{100} (nm) in 0.1 mol L^{-1} $KClO_4$**
- 400	1.73	- 250	-*	- 600	2.09
+ 250	1.89	+ 250	2.65	+ 300	2.10
+ 600	2.23	+ 750	2.76	+ 600	2.07

*Diffraction peak inaccessible due to de-doping induced disorder.

References

1 M. Moser, T. C. Hidalgo, J. Surgailis, J. Gladisch, S. Ghosh, R. Sheelamanthula, Q. Thiburce, A. Giovannitti, A. Salleo, N. Gasparini, A. Wadsworth, I. Zozoulenko, M. Berggren, E. Stavrinidou, S. Inal and I. McCulloch, *Advanced Materials*, DOI:10.1002/adma.202002748.

2 A. E. Ross, D. G. McCulloch and D. R. McKenzie, *Acta Crystallogr A Found Adv*, 2020, **76**, 468–473.

3 R. K. Hallani, B. D. Paulsen, A. J. Petty, R. Sheelamanthula, M. Moser, K. J. Thorley, W. Sohn, R. B. Rashid, A. Savva, S. Moro, J. P. Parker, O. Drury, M. Alsufyani, M. Neophytou, J. Kosco, S. Inal, G. Costantini, J. Rivnay and I. McCulloch, *J. Am. Chem. Soc.*, 2021, **143**, 11007–11018.

4 V. Lemaur, L. Muccioli, C. Zannoni, D. Beljonne, R. Lazzaroni, J. Cornil and Y. Olivier, *Macromolecules*, 2013, **46**, 8171–8178.

5 V. Lemaur, J. Cornil, R. Lazzaroni, H. Sirringhaus, D. Beljonne and Y. Olivier, *Chem. Mater.*, 2019, **31**, 6889–6899.

6 S. R. Chaudhari, J. M. Griffin, K. Broch, A. Lesage, V. Lemaur, D. Dudenko, Y. Olivier, H. Sirringhaus, L. Emsley and C. P. Grey, *Chem. Sci.*, 2017, **8**, 3126–3136.

7 J.-P. Ryckaert, G. Ciccotti and H. J. Berendsen, *Journal of Computational Physics*, 1977, **23**, 327–341.

8 A. P. Thompson, H. M. Aktulga, R. Berger, D. S. Bolintineanu, W. M. Brown, P. S. Crozier, P. J. In ’T Veld, A. Kohlmeyer, S. G. Moore, T. D. Nguyen, R. Shan, M. J. Stevens, J. Tranchida, C. Trott and S. J. Plimpton, *Computer Physics Communications*, 2022, **271**, 108171.

9 R. Gowers, M. Linke, J. Barnoud, T. Reddy, M. Melo, S. Seyler, J. Domański, D. Dotson, S. Buchoux, I. Kenney and O. Beckstein, Austin, Texas, 2016, pp. 98–105.

10 N. Michaud-Agrawal, E. J. Denning, T. B. Woolf and O. Beckstein, *J Comput Chem*, 2011, **32**, 2319–2327.

11 A. Stukowski, *Modelling Simul. Mater. Sci. Eng.*, 2010, **18**, 015012.

12 R. Skånberg, I. Hotz, A. Ynnerman and M. Linares, *J. Chem. Inf. Model.*, 2023, **63**, 7382–7391.

13 B. L. Henke, E. M. Gullikson and J. C. Davis, *Atomic Data and Nuclear Data Tables*, 1993, **54**, 181–342.

14 M. Newville, *J. Phys.: Conf. Ser.*, 2013, **430**, 012007.